Probing electron-electron interaction along with superconducting fluctuations in disordered TiN thin films

Sachin Yadav [1,2] Vinay Kaushik [3] M. P. Saravanan,[3] and Sangeeta Sahoo [1,2,*]

[1]*CSIR-National Physical Laboratory, Dr. K. S. Krishnan Marg, New Delhi 110012, India*
[2]*Academy of Scientific and Innovative Research (AcSIR), Ghaziabad 201002, India*
[3]*Low Temperature Laboratory, UGC-DAE Consortium for Scientific Research, University Campus,*
Khandwa Road, Indore 452001, India

In two-dimensional (2D) disordered superconductors prior to superconducting (SC) transition, the appearance of a resistance peak in the temperature dependent resistance $R(T)$ measurements indicates the presence of weak localization (WL) and electron-electron interaction (EEI) in the diffusion channel and SC fluctuations in the Cooper channel. Here, we demonstrate an interplay between SC fluctuations and EEI by low-temperature magnetotransport measurements for a set of 2D disordered TiN thin films. While cooling the sample, a characteristic temperature T^* is obtained from the $R(T)$ at which SC fluctuations start to appear. The upturn in $R(T)$ above T^* corresponds to WL and/or EEI. By the temperature and field dependences of the observed resistance, we show that the upturn in $R(T)$ originates mainly from EEI with a negligible contribution from WL. Further, we have used the modified Larkin's electron-electron attraction strength $\beta(T/T_c)$, containing a field-induced pair-breaking parameter, in the Maki-Thompson SC fluctuation term. Here, the temperature dependence of $\beta(T/T_c)$ obtained from the magnetoresistance (MR) analysis shows a diverging behavior close to T_c, and it remains almost constant at higher temperature within the limit of $\ln(T/T_c) < 1$. Interestingly, the variation of $\beta(T/T_c)$ on the reduced temperature (T/T_c) offers a common trend which has been closely followed by all the concerned samples presented in this paper. Finally, the temperature dependence of inverse phase scattering time (τ_ϕ^{-1}), as obtained from the MR analysis, clearly shows two different regimes; the first one close to T_c follows the Ginzburg-Landau relaxation rate (τ_{GL}^{-1}), whereas the second one at high temperature varies almost linearly with temperature, indicating the dominance of inelastic electron-electron scattering for the dephasing mechanism. These two regimes are followed in a generic way by all the samples despite being grown under different growth conditions.

I. INTRODUCTION

In a superconductor, the transition from the metallic state occurs in two phases: First, the order parameter is established with a finite amplitude at the critical temperature (T_c), and then the formation of the global phase coherent state at the characteristic temperature T_{BKT} occurs [1–3]. In two-dimensional (2D) disordered superconductors above T_c, electrical transport properties are mainly controlled by the quantum corrections to the conductivity (QCCs) [4,5]. The QCC can broadly be summarized into two parts: First is the weak localization (WL) due to quantum interference of complementary electron waves travelling in a closed loop but opposite in direction, and second is the disorder-induced electron-electron interaction (EEI) [6–8]. Further, quantum corrections originating from EEI can be divided into two parts: The first part includes Coulomb interaction between the particles with close momenta in the diffusion channel (ID), and the second part includes Coulomb interaction between the particles having opposite momenta in the Cooper channel. Correction to the conductivity due

to the Cooper channel becomes important once the system transits to a superconducting (SC) state. However, corrections to the conductivity arising from the channel of the Cooper pairs are further divided into three SC fluctuations, namely, Aslamazov-Larkin (AL) contribution which is mainly due to the participation of Cooper pairs in conduction through parallel channel [9], Maki-Thompson (MT) contribution which reflects the influence of SC fluctuations on normal quasiparticles [10,11], and density of states (DOS) contribution which originates due to the formation of SC pairs that lead to the reduction in the DOS for normal electrons [12]. Here, SC fluctuations related to AL and MT give positive contributions, and DOS gives negative contribution to the conductivity under zero magnetic field [13], whereas WL + ID together offers a negative contribution to the conductivity. However, SC fluctuations and WL are very sensitive to the magnetic field, and they get suppressed under the application of magnetic field, whereas the contribution from the EEI remains unaffected under a high magnetic field [14].

In this paper, we have studied an interplay between SC fluctuations in the Cooper channel and EEI in the electronic diffusion channel by low-temperature magnetotransport measurements for a set of disordered TiN thin film samples that

*sahoos@nplindia.org

014511-1

are in the 2D limit. A detailed study using all the aforesaid quantum corrections to the conductivity is reported by Baturina *et al.* [13] for disordered SC TiN thin films of thickness in the same range (<5 nm) as that of the samples presented in this paper. The observations and conclusions on the zero-field $R(T)$ measurements for this paper closely follow the reported results from Ref. [13]. However, the study presented here extends up to an advanced level where an external magnetic field, applied perpendicular to the sample plane, is used to probe only the EEI by suppressing the other relevant mechanism like WL which may lead to an upturn in zero-field $R(T)$ measurements. By the analysis of magnetoresistance (MR) results, we show here that indeed EEI is dominant for these SC films above the transition temperature.

Here, samples are produced by using the previously demonstrated substrate-mediated nitridation technique where the annealing temperature and the film thickness were varied. The set of samples selected for this paper includes samples grown with different annealing temperatures and samples varying in film thickness. However, the results from the transport measurements carried out on these varieties of samples follow similar characteristics when we consider the temperature-dependent resistance measurements $R(T)$ and/or the MR measurements. For example, while cooling from room temperature, zero-field $R(T)$ characteristics for all the samples feature a resistance dip at a specific temperature T_{min} which is then followed by an upturn with negative dR/dT slope and finally reaching a resistance peak at temperature T_{max}, and further cooling leads to a superconductivity-related drop in resistance. All these distinct regions, characterized mainly by the sign of the slope dR/dT, are present in zero-field $R(T)$ for each of the samples presented here. Further, we have obtained the characteristic temperature T^* at which SC fluctuations start to appear and the experimental $R(T)$ starts to deviate from the WL + ID path. The characteristic temperatures T^*, T_{max}, and T_{min} and the resistance peak have been explicitly monitored with respect to magnetic field, and we find that the contribution from WL to the QCC is very weak compared with that from EEI, and hence, EEI can be considered the main mechanism behind the upturn and the resistance peak observed in $R(T)$. Further, the MR measurements show positive MR at temperature far above T_c, and no trace of negative MR is observed even above T^* where SC fluctuations can be ignored. As negative MR is a hallmark for WL [15], MR measurements too indicate that the contribution from WL is not significant.

As far as the SC fluctuations are concerned, above T_c, the MT correction is the most dominant contribution to QCC. The strength of the MT contribution is generally expressed by the electron-electron attraction strength $\beta(T/T_c)$ which was proposed by Larkin [16]. Here, $\beta(T/T_c)$ varies differently for $[\ln(T/T_c) \ll 1]$ and $[\ln(T/T_c) \gg 1]$. However, it is problematic to evaluate the value of $\beta(T/T_c)$ in the intermediate temperature regime, and in this regime, no clear report or guidance about the form of $\beta(T/T_c)$ is available in the literature. However, a modified magnetic-field-dependent $\beta(T/T_c)$ has been proposed by Lopes dos Santos and Abrahams [17] which is valid for the low-temperature regime. In this paper, we have considered the modified $\beta(T/T_c)$ which depends on a pair-breaking parameter δ via the phase scattering time (τ_ϕ)

which is obtained from the MR analysis. The dependence of $\beta(T/T_c)$ on the reduced temperature (T/T_c) shows a diverging behavior close to T_c, whereas it behaves almost independent of temperature for the regime which is a little far from T_c but still satisfying the condition $[\ln(T/T_c) < 1]$. Interestingly, the variation of $\beta(T/T_c)$ on T/T_c offers a common path which is followed by all the samples in a collective or universal manner. Furthermore, the inverse phase relaxation time (τ_ϕ^{-1}) as obtained from the MR varies generically on reduced temperature (T/T_c) for all the samples. Close to T_c, SC fluctuations dominate, and τ_ϕ^{-1} follows the Ginzburg-Landau (GL) relaxation rate (τ_{GL}^{-1}), and at higher temperature, the phase relaxation time varies almost linearly with temperature, indicating the dominance of inelastic electron-electron scattering for the dephasing mechanism.

II. EXPERIMENTAL

We have employed an undoped Si (100) substrate covered with an 80-nm Si_3N_4 dielectric spacer layer grown by low-pressure chemical vapor deposition. Initially, substrates went through the standard cleaning process involving sonication in an acetone and isopropanol bath for 15 min each. Thereafter, cleaned substrates were loaded into the ultrahigh vacuum (UHV) chamber for preheating at $\sim 820\,°C$ for 30 min to remove adsorbed or trapped organic molecules on the surface of the substrate. The cleaned substrates were then transferred *in situ* to the sputtering chamber where a thin layer of Ti was deposited on the substrate by using dc magnetron sputtering of the Ti target (99.999% purity) in the presence of high-purity Ar (99.9999%) gas. Sputtering of the Ti target was done with the base pressure $<1.5 \times 10^{-7}$ Torr. Finally, Ti-deposited substrates were transferred *in situ* to an UHV chamber for annealing. Ti thin-film-deposited substrates were annealed at different annealing temperatures of ~ 820, ~ 780, and $\sim 750\,°C$ for 2 h at a pressure $<5 \times 10^{-8}$ Torr. During the annealing process, Ti transformed into TiN by the substrate-mediated nitridation technique [18–21] where the Si_3N_4 substrate decomposed into Si (s) and N (g) atoms, and due to high affinity of titanium toward both, formation of SC TiN as the majority phase along with the non-SC minority phase $TiSi_2$ took place. However, more detail about the substrate-mediated nitridation technique has been reported elsewhere [20]. For carrying out the electrical transport measurements at low temperature, TiN thin-film-based multiterminal devices were fabricated by using a stainless-steel shadow mask to pattern the TiN thin-film-based SC channel. We have used a complimentary separate shadow mask to make the contact leads for voltage and current probes. The contact leads were made of Au (80–100 nm)/Ti (5 nm) deposited by dc magnetron sputtering. Low-temperature resistivity measurements were carried out using a 16 T/2 K Physical Properties Measurement System (PPMS) of Quantum Design, USA at UGC-DAE CSR Indore with an excitation of 100 nA. The morphological characterizations of the samples were performed by using atomic force microscope (AFM) from BRUKER, Dimension ICON, in tapping mode from IIT, Mandi, India.
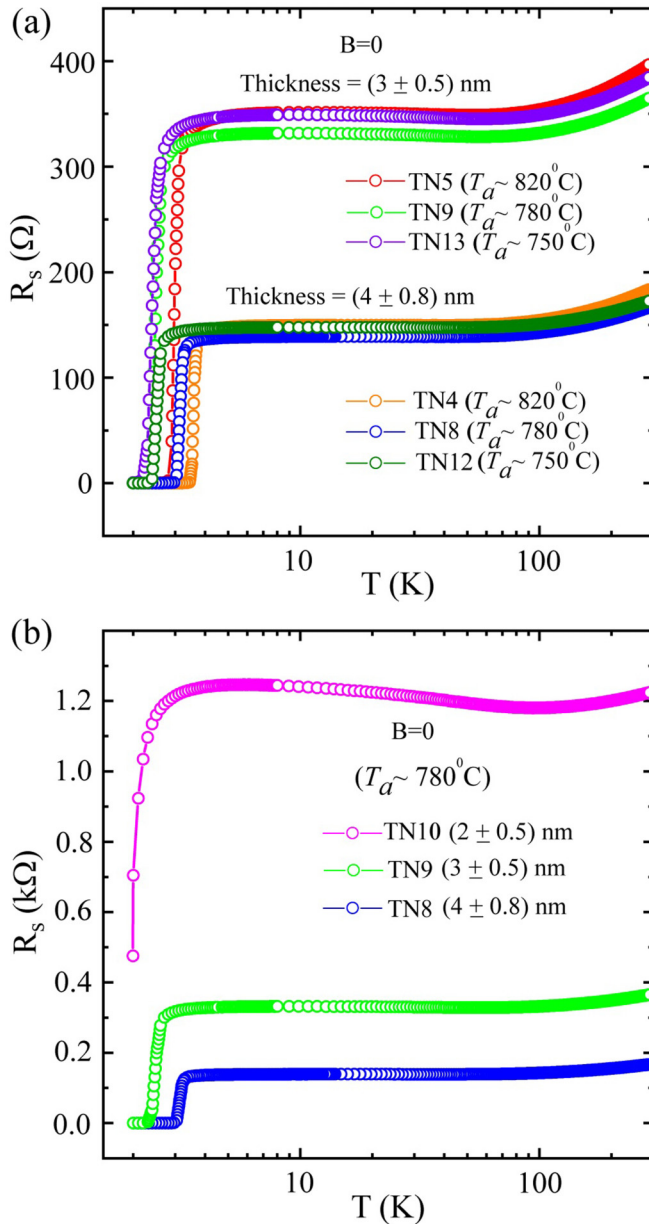
FIG. 1. Semilogarithmic presentation of temperature-dependent resistance $R(T)$ characteristics for TiN thin films having different annealing temperature (T_a) and film thickness. Here, resistance R_s is in Ω/sq. (a) Two sets of zero-field $R(T)$ characteristics measured from room temperature down to 2 K with each set containing three different samples of the same thickness but with different annealing temperature. (b) Transport properties of three samples grown at the same annealing temperature but different film thicknesses.

III. RESULTS AND DISCUSSION

Temperature-dependent resistance $R(T)$ measurements have been carried out on TiN thin films with dimensions of 1100 μm (length) × 500 μm (width) by using the conventional four-probe geometry. Further, to investigate the role of annealing temperature (T_a) and film thickness on the transport properties, we have fabricated TiN thin films by keeping one growth parameter fixed and altering the other. In Fig. 1(a), we present the zero-field $R(T)$ characteristics of six different

samples from room temperature down to 2 K in a semilog-arithmic scale. Based on the influence of the film thickness on the electronic properties, $R(T)$'s of these six TiN thin film samples are divided into two sets, where one set of $R(T)$'s belongs to the film thickness of ∼3 nm, and the other set corresponds to 4 nm, as indicated in Fig. 1(a). We have observed that the variations in T_a from 820 to 750 °C (TN4, TN8, and TN12) while keeping the film thickness fixed at ∼4 nm have very little influence on the normal state resistance (R_N), and corresponding $R(T)$'s almost overlap with each other in their normal state. Similar behavior is observed for the film thickness of ∼3 nm, where all the related $R(T)$ characteristics (TN5, TN9, and TN13) show resemblance in their R_N and its variation from room temperature down to the temperature just before transiting to the SC state. In Fig. 1(a), a change in the film thickness from 4 to 3 nm shows a significant change in the R_N for any T_a (820, 780, or 750 °C) considered here. Therefore, particularly in the normal state, variation in the film thickness has a greater influence on the transport properties than the influence of T_a. However, SC properties such as critical temperature (T_c) and transition width depend strongly on T_a as is apparent from Fig. 1(a), where the normal metallic-to-superconductor transition shifts toward lower temperature with broader transition width for reducing T_a from 820 to 780 °C and further to 750 °C. To observe the effect of thickness on the overall transport properties, we have collected a set of $R(T)$ measurements for three samples TN8, TN9, and TN10 having different film thicknesses of ∼4, 3, and 2 nm, respectively, and grown with a fixed T_a of ∼780 °C, as shown in Fig. 1(b). With the reduction in the film thickness, R_N starts to increase while T_c shifts toward the lower temperature side. Here, samples TN8 and TN9 undergo a complete superconductivity; however, with a reduction in the film thickness from 3 to 2 nm, sample TN10 shows partial superconductivity, as observed in Fig. 1(b). Further, we have investigated the zero-field $R(T)$ characteristics in more detail for the set of samples (TN8, TN9, and TN10) presented in Fig. 1(b). A narrow temperature window for $R(T)$ is considered for each of the samples in this set for emphasizing the close vicinity of the metal-superconductor transition, and they are shown in the main panels of Figs. 2(a)–2(c). The details about the $R(T)$ variation in the normal state for all three samples are highlighted in the insets of Figs. 2(a)–2(c), which show different regions mainly based on the slope dR/dT from the measured $R(T)$. For all the samples, while cooling down from room temperature, resistance decreases with decreasing temperature until it reaches a minimum at the characteristic temperature T_{min}, indicating metallic behavior with positive dR/dT. Further lowering the temperature, an upturn in $R(T)$ appears where resistance starts to increase and reaches a maximum at the temperature T_{max}. In this regime between T_{min} and T_{max}, the negative dR/dT indicates an insulating or semiconducting type of behavior. At temperature below T_{max}, resistance drops sharply, and the SC fluctuations take over. For example, the thinnest sample TN10 with ∼2 nm thickness shows metallic behavior with positive dR/dT at $T > T_{min} = 95$ K and an upturn accompanied by a resistance peak with negative dR/dT for the temperature window from 95 to 5.8 K ($T_{max} \sim 5.8$ K), as shown in Fig. 2(a). Finally, < 5.8 K (T_{max}),
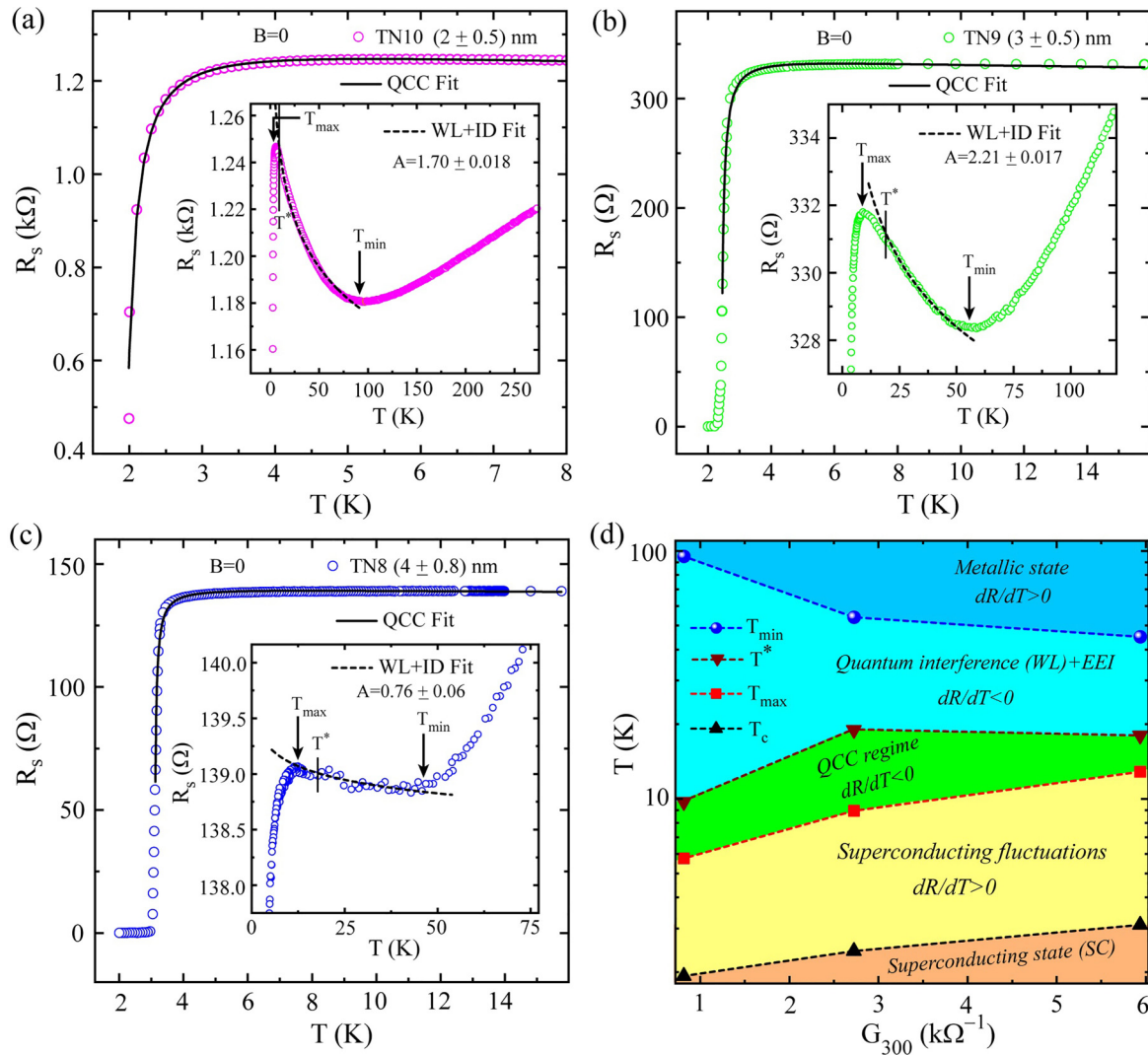
FIG. 2. Investigation of zero-field $R(T)$ data in more detail by using quantum correction to the conductivity (QCC) theory for individual TiN thin films grown at the same annealing temperature ($T_a = 780\,^\circ$C) but with different thicknesses. (a)–(c) Main panels: QCC fitting to $R(T)$ data for a selective range of temperature in the vicinity of the normal metal-to-superconductor transition. Insets: $R(T)$ for a wider range of temperature demonstrating an upturn with a maximum in resistance appearing at T_{max} as well as a minimum in resistance at T_{min}. T_{max} represents the onset of resistance drop causing the superconducting (SC) transition, and T_{min} represents the deviation from the metallic behavior on further lowering the temperature. The region between T_{min} and T_{max} is fitted with [weak localization (WL)+interaction between the particles with close momenta in the diffusion channel (ID)] model as shown by the black dashed curves. (d) Temperature-conductance phase diagram constructed by the characteristic temperatures and conductance measured at 300 K for the samples shown in (a)–(c). With the help of the characteristic temperatures T_{min}, T_{max}, T_c, and T^*, different regimes from metallic state to SC state are defined and highlighted in the phase diagram. T_{min}, T_{max}, and T^* are shown in the insets of (a)–(c), where T_{max} and T_{min} correspond to the temperature points with maximum and minimum resistance, respectively, and T^* is the temperature point just above the T_{max} at which (WL+ID) fit starts to deviate from the experimental data. Here, T_c values are extracted from the QCC fitting performed on the $R(T)$ data for individual samples.

resistance starts to drop sharply as the sample transits to a SC state.

Similarly, while cooling from room temperature, a resistance minimum followed by an upturn and SC drop appear in $R(T)$ for the other two samples (TN9 and TN8), as displayed in the insets of Figs. 2(b) and 2(c), respectively. Here, the slope of the upturn increases with decreasing film thickness. This is expected when EEI plays the dominant role, as reduction in thickness introduces more disorder, and EEI increases with disorder. An upturn in resistance can originate from granularity also. However, for the granular SC systems,

no systematic reduction in T_c occurs for decreasing thickness [22], but in this paper, as shown in Fig. 1(c) and also in Table I, we observe that T_c decreases systematically with the decreasing thickness, and at the same time, the transitions remain sharp. This indicates the granularity might not be the reason behind the observed upturn in the zero-field $R(T)$ [23]. Further, the surface morphology, as observed through AFM images shown in Fig. S7 in the Supplemental Material (SM) [24], does not clearly indicate the granular nature of the films, as the images reflect the surface roughness rather than isolated grains.

TABLE I. Specific parameters for the samples presented in this paper.

Samples	T_a (°C) $\pm 10\,°C$	d (nm)	T_c (K) (QCC) fit	R_{max} (Ω)	R_n^{300K} (Ω)	$B_{c2}(0)$ (T)	D (cm^2 s^{-1})	l_T (100 K) (nm)
TN4	820	4 ± 0.8	3.55	150	186	4.41	0.612	13
TN5	820	3 ± 0.5	2.93	352	400	5.5	0.405	11
TN8	780	4 ± 0.8	3.1	139	168	4.0	0.589	13
TN9	780	3 ± 0.5	2.43	332	367	4.31	0.429	11
TN10	780	2 ± 0.5	1.93	1246	1227	6.0	0.245	9
TN12	750	4 ± 0.8	2.47	148	174	3.31	0.567	13
TN13	750	3 ± 0.5	2.35	349	386	4.41	0.405	11

Generally, WL and EEI play major roles for the appearance of the resistance peak and upturn in $R(T)$ for 2D homogeneously disordered materials [4,8,25,26]. However, the dimensionality of the system is very sensitive to WL, EEI, and SC fluctuations; therefore, characteristic length scales such as the SC coherence length $\xi_{GL}(0) = [\frac{\phi_0}{2\pi T_c |\frac{dH_{c2}}{dT}|_{T_c}}]^{1/2}$, with ϕ_0 as the flux quantum, and thermal coherence length $L_T = \sqrt{2\pi \hbar D/(k_B T)}$, with k_B as the Boltzmann constant and D as the diffusion coefficient, should be less than the film thickness. Moreover, for all the samples presented here, the film thickness is less than the characteristic SC coherence length ($\sim$9 nm) and the thermal coherence length ($\sim$9 to $\sim$13 nm at 100 K). Therefore, quantum corrections to the conductivity that are applicable in 2D materials can be considered here for understanding the origin of the upturn and the related resistance peak appearing in the zero-field $R(T)$ characteristics. Furthermore, the sample-specific characteristic parameters like T_a, film thickness (d), sheet resistance (R_{max}) at T_{max} before SC transition, SC critical temperature (T_c) as obtained by QCC fit, sheet resistance at 300 K ($R_{300\,K}$), upper critical field at $T = 0\,$K[$B_{c2}(0)$], diffusion constant (D), and the thermal coherence length (L_T) at 100 K for all the TiN samples are listed in Table I.

Further, the presence of non-SC minority phases like TiSi$_2$ and elemental Si in these substrate-mediated TiN thin films [19] induces disorder, and disordered 2D systems are ideal candidates where WL and EEI in the diffusion channel (ID) play prominent roles for the appearance of an upturn and corresponding resistive peak at T_{max} in the zero-field $R(T)$. Inclined to this, we have followed here the 2D treatment with WL and EEI to address the observed upturn in the zero-field $R(T)$.

In the 2D case, WL and EEI (ID) contributions to the conductivity can be obtained as [12,26]

$$\frac{\Delta G^{WL}(T) + \Delta G^{ID}(T)}{G_{00}} = A \ln\left(\frac{k_B T \tau}{\hbar}\right), \qquad (1)$$

$$R(T) = \frac{1}{[\Delta G^{WL}(T) + \Delta G^{ID}(T)] + 1/R(T = 10\,K)}, \qquad (2)$$

with $G_{00} = e^2/(2\pi^2 \hbar)$. Here, A is a proportional constant, and τ is the electron mean free time, and they are considered as fitting parameters. From Eq. (1), corrections due to both WL and EEI to the conductivity vary logarithmically with the temperature, and accordingly, the experimental $R(T)$ data for

the temperature window from T_{max} to T_{min} are fitted by using Eq. (2). The related fits in the upturn region with negative dR/dT are shown by the solid cyan curves in the insets of Figs. 2(a)–2(c) for the aforementioned three samples TN10, TN9, and TN8, respectively. The fitted curves (black dashed curves) show reasonably good agreement with the experimental data, indicating the possibility of WL and EEI (ID) being responsible for the observed upturn and the resistance peak in the $R(T)$. The extracted values of A from the fitting for all the samples are <3 which is expected for the homogenously disordered thin films [26]. Interestingly, if we look into more detail at the WL+ID fitting from T_{min} to T_{max}, we observe that the fit deviates from the experimental points before reaching T_{max}. The temperature at the deviation point is marked as T^*, and the vertical dashed lines in the insets of Figs. 2(a)–2(c) correspond to T^*, which occur at 9.8, 19, and 18 K for the samples TN10, TN9, and TN8, respectively. The deviation point is very clear in the inset of Fig. 2(b) for the sample TN9. The deviation relates to the onset of SC fluctuations that start to contribute to the conductivity corrections along with WL and EEI. Therefore, the region between T^* and T_{max} shows the possibility of the coexistence of SC fluctuations, mainly the MT contributions, along with some contribution from WL and EEI. Close to T_c, SC fluctuation related to the AL term contributes significantly in addition to the MT [9–11]. Further, the reduction in DOS due to the Cooper pair formation contributes also to the SC fluctuations [12]. Therefore, the relevant contributions from SC fluctuations are [9–12]

$$\frac{\Delta G^{AL}(T)}{G_{00}} = \frac{\pi^2}{8}\left[\ln\left(\frac{T}{T_c}\right)\right]^{-1}, \qquad (3)$$

$$\frac{\Delta G^{MT}(T)}{G_{00}} = \beta\left(\frac{T}{T_c}\right)\ln\left(\frac{k_B T \tau_\phi}{\hbar}\right), \qquad (4)$$

$$\frac{\Delta G^{DOS}(T)}{G_{00}} = \ln\left[\frac{\ln(T_c/T)}{\ln(k_B T_c \tau/\hbar)}\right]. \qquad (5)$$

Here, τ_ϕ introduces phase-breaking processes due to mainly inelastic scattering (as spin-flip scattering can be ignored) [27,28], and $\beta(T/T_c)$ relates to the strength function characterizing EEI which has been introduced by Larkin [16]. Summing up all the contributions related to the total QCCs, the experimental data from T^* (deviation point from WL+ID fitting) to the lowest available temperature can be fitted by
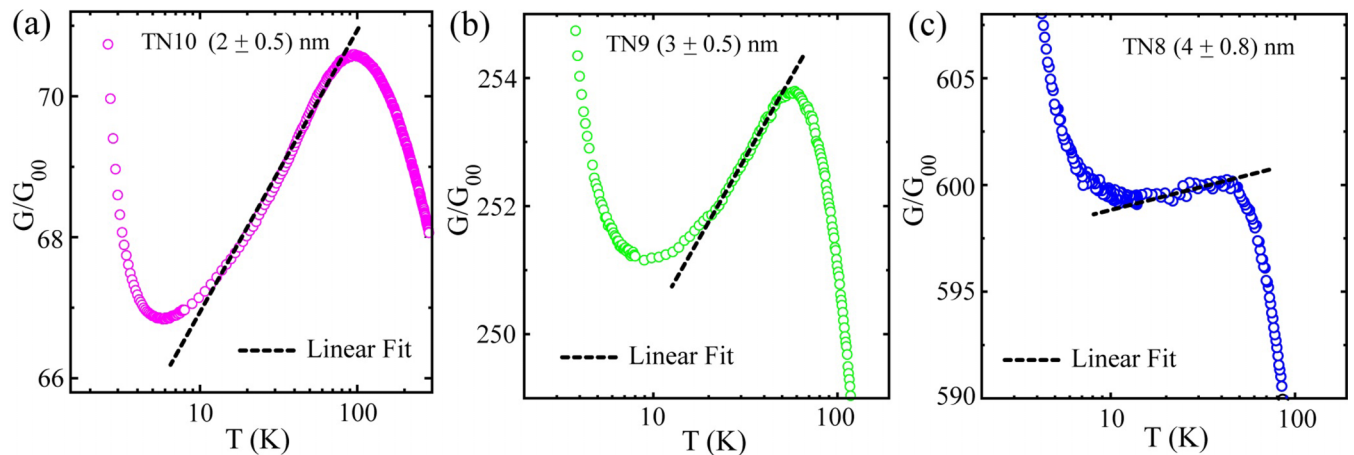
FIG. 3. Logarithmic temperature dependence of conductance presented in semilogarithmic scale for the samples TN10, TN9, and TN8 in (a)–(c), respectively. The black dashed lines are the linear fit to the experimental data.

using the following equation:

$$R(T) = \frac{1}{[\Delta G^{\mathrm{WL}}(T) + \Delta G^{\mathrm{ID}}(T) + \Delta G^{\mathrm{AL}}(T) + \Delta G^{\mathrm{DOS}}(T) + \Delta G^{\mathrm{MT}}(T)] + 1/R(T = 10\,\mathrm{K})}. \tag{6}$$

The black solid curves are the fits to the experimental data by using Eq. (6) for the samples TN10, TN9, and TN8, as shown in Figs. 2(a)–2(c), respectively. The fits follow the experimental data nicely, indicating the existence of SC fluctuations (mainly MT) above $T_{\max}$ along with the quantum interference (WL) and EEI. However, the contribution of WL+EEI cannot be neglected in the region from T^{*} to $T_{\max}$, though this region is mainly dominated by SC fluctuations. The SC critical temperature (T_c) is obtained from the MT contribution in the QCC fitting [10,11]. Moreover, the samples belonging to other T_a's (820 and 750 °C) demonstrate the same behavior in $R(T)$ as that observed for $T_a = 780$ °C, and the corresponding $R(T)$ fittings by using Eq. (6) are shown in Fig. S1 in the SM [24]. Finally, the characteristic temperature points such as $T_{\min}$, $T_{\max}$, and T^{*} are extracted from the $R(T)$ data presented in Figs. 2(a)–2(c) along with T_c from the QCC fit and plotted in Fig. 2(d) against sample conductance measured at 300 K. Initially, resistance follows linearly with temperature ($R \propto T$) from room temperature to $T_{\min}$, where dR/dT becomes positive and marked as a metallic state. Further, by lowering the temperature from $T_{\min}$, resistance deviates from the linear behavior and starts to rise, and dR/dT becomes negative until $T_{\max}$. However, this rise in resistance with the decrease in temperature is mainly dominated by WL and EEI until T^{*}, and below T^{*}, theoretical fitting of (WL+ID) starts to deviate; therefore, this region from $T_{\min}$ to T^{*} is marked as a quantum interference (WL) and EEI regime in Fig. 2(d). Furthermore, the region from T^{*} to $T_{\max}$ is marked as the QCC regime, where combinedly SC fluctuations and quantum interference contribute to total quantum correction to the conductivity. However, the region from $T_{\max}$ to T_c, where dR/dT again becomes positive, is mainly dominated by SC fluctuations, and below T_c, the state is marked as the SC state. Summarizing, the full-scale $R(T)$ from 300 down to 2 K is divided into four distinct regimes,

starting from the metallic state (the light blue region) to the WL+EEI regime (the cyan region) to QCC (the green region) to SC fluctuations (the yellow region) to, finally, the SC state (the orange color). Further, the data in Fig. 1(b) are replotted with respect to the dimensionless conductance G/G_{00} in Fig. 3 by using a semilogarithmic scale. The logarithmic temperature dependence of conductance, as shown in Fig. 3, confirms the two dimensionality of the samples considered in this paper [8,29] and rules out the three-dimensional theory, where conductance G varies with temperature T as $G \propto \sqrt{T}$ [30]. The logarithmic temperature dependence of conductance is the signature for the presence of WL and EEI in 2D systems [8,29], and similar behavior is also observed for the samples annealed at 820 and 750 °C, as shown in the SM (Fig. S2) [24]. The linear fits (black dashed lines) marked in Fig. 3 show the deviation from the linearity ∼10 K for the sample TN10 and ∼18 K for samples TN9 and TN8, and these deviation points in temperature resemble the value of T^{*}, shown in Figs. 2(a)–2(c), as obtained by the fit for WL+ID contribution to the conductivity theory.

$R(T)$ measurements under perpendicular magnetic field

As a quantum interference phenomenon like WL is very sensitive to the magnetic field, we have carried out $R(T)$ measurements in the presence of magnetic field applied perpendicular to the sample plane. External magnetic field can be used as a tool to distinguish the quantum phenomena WL and EEI through MR and $R(T)$ measurements. When $R(T)$ measurements are carried out under perpendicular magnetic field, a relatively small field can destroy the WL effect, but the contribution from EEI remains unaffected [14]. As already discussed, in 2D, zero-field resistance depends logarithmically on temperature for both WL and EEI. However, with the application of magnetic field, EEI is only responsible for
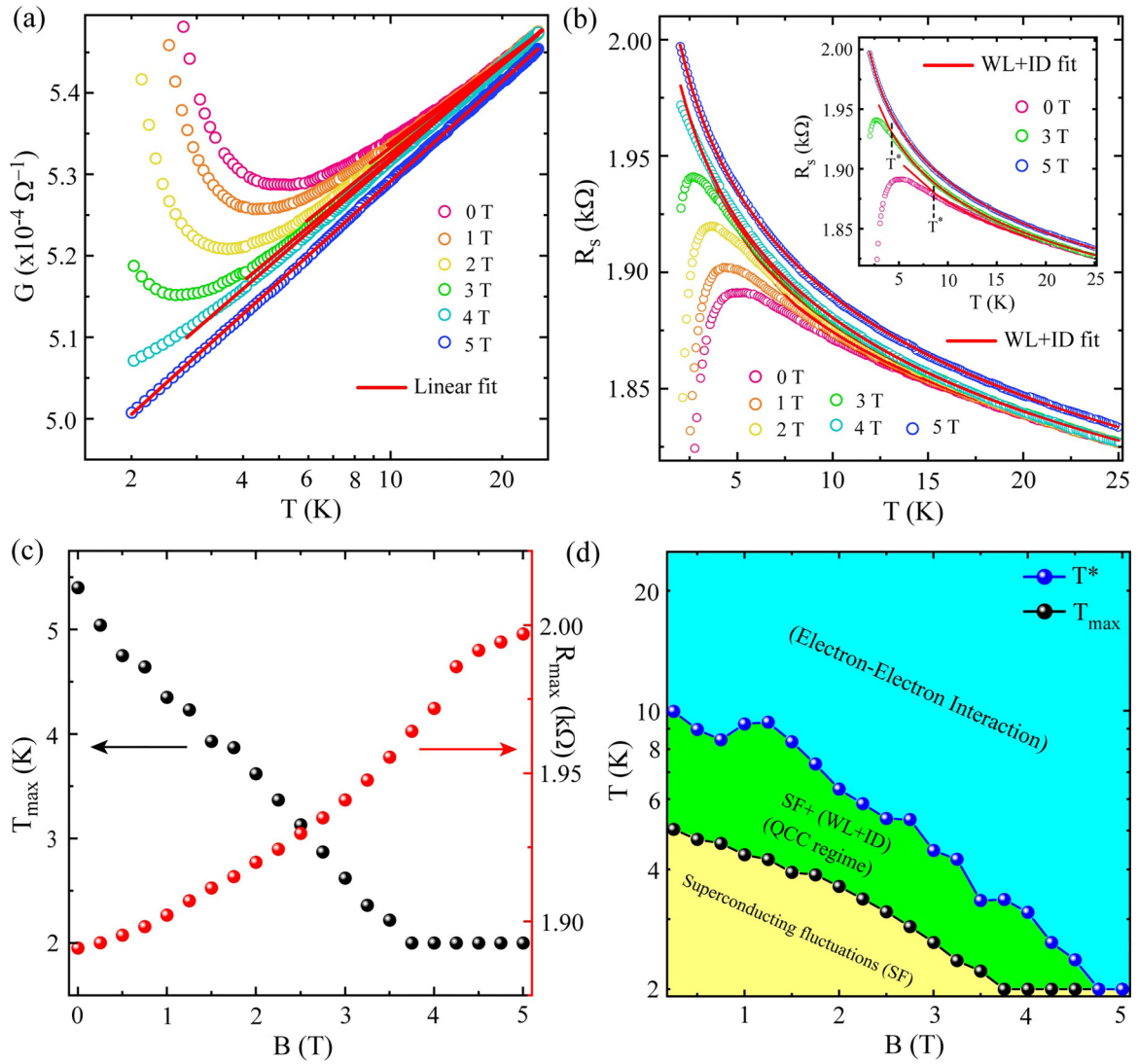
FIG. 4. Field-dependent $R(T)$ measurements for the sample TN10A (from the same batch of TN10) with magnetic field applied perpendicular to the sample plane. (a) Temperature dependence of conductance (G) in semilogarithmic scale under various applied magnetic field. The red solid lines are the linear fits indicating that the temperature dependence for the conductance remains logarithmic even after applying magnetic field. (b) Corresponding $R(T)$ measured under the magnetic field as mentioned in (a). The field-dependent $R(T)$'s are fitted with the contribution from [weak localization (WL)+interaction between the particles with close momenta in the diffusion channel (ID)] theory by using Eq. (2), and the fits are shown by the solid red curves. Inset: Three selective $R(T)$'s measured under 0, 3, and 5 T from the main panel for a clearer view. For each field, the deviation of the WL+ID fit from the experimental data occurs at T^*, which is marked by the dashed vertical line. (c) The variation of T_{max} and the corresponding maximum resistance value with the applied magnetic field. Here, the saturation in T_{max} after 3.75 T appears due to the temperature limitation of the measuring instrument which is limited by 2 K as the lowest achievable temperature. (d) B-T phase diagram obtained from the extracted T^* and T_{max} from the field-dependent $R(T)$ data.

logarithmic $R(T)$ dependence, as magnetic field destroys WL [14]. Here, to find out the actual mechanism behind the upturn observed in $R(T)$ and to find out the contribution only from EEI, we have carried out $R(T)$ measurements under external magnetic field for a sample (TN10A) selected from the same batch of TN10, and the corresponding field-dependent $R(T)$ is shown in Fig. 4.

First, we have considered the temperature dependence of conductance $G(1/R_s)$ measured under external magnetic field, and the same is presented in Fig. 4(a) using a semilogarithmic scale. The excellent agreement with the experimental data by the linear fits as presented by the red solid lines confirm the logarithmic temperature dependence for the con-

ductance which becomes more prominent with increasing field. Due to the presence of SC fluctuations at relatively lower magnetic fields (1, 2, and 3 T), linear fit follows the experimental points at the higher temperature region and deviates at T^*, whereas for higher magnetic field, the linear fit follows almost the entire experimental range down to the lowest temperature (∼2 K). The dominance of logarithmic temperature dependence for conductance at higher magnetic field indicates the presence of EEI. Further, to observe a clear distinction between T_{max} and T^* under an external magnetic field, we have presented the corresponding $R(T)$ in Fig. 4(b) by using a linear scale representation. For the applied field up to 3 T, resistance drop related to superconductivity is

observed, whereas at 4 T and above, resistance continues to increase with temperature down to the lowest accessible temperature 2 K, indicating an insulating type of behavior, as evident from Fig. 4(b). Here, we have fitted the resistive upturn from 25 K to the lower temperature regime by using Eq. (2) which deals with WL+ID correction for 2D disordered metal, and the fits are represented by the red solid curves. For clarity, three representative $R(T)$'s measured at 0, 3, and 5 T are shown selectively in the inset of Fig. 4(b). Here, the deviation of the WL+ID fit from the experimental data is evident for 0 and 3 T, and the related temperature T^* is marked by the vertical dashed lines. However, for the 5 T field, the fit extends the whole experimental range down to the lowest temperature (2 K). Therefore, T^* shifts toward lower temperature with increasing magnetic field. Here, the upturn region from T^* to $T_{\max}$ can be attributed to the presence of SC fluctuations along with WL and EEI contributions. Further, when T^* is not distinguishable from $T_{\max}$ as in the case of higher field, the magnetic field destroys SC fluctuations and WL contribution, but EEI remains prominent, and the upturn in $R(T)$ gets stronger. Therefore, at high magnetic field (5 T), the upturn region from $T_{\min}$ to $T_{\max}$ is mainly due to the presence of EEI.

Further, $T_{\max}$ and its respective resistance values under the presence of an external magnetic field are displayed in Fig. 4(c). As observed in Fig. 4(b), with increasing magnetic field, $T_{\max}$ shifts toward lower temperature. Above 3.75 T, $T_{\max}$ gets saturated at 2 K due to the limitation in the measurement temperature as the lowest accessible temperature of the system is 2 K, whereas the resistance at $T_{\max}$ shows a reverse trend with the magnetic field and reaches the maximum value $\sim$2 kΩ at 5 T at the lowest temperature 2 K. Increment in the resistance value at $T_{\max}$ with magnetic field is opposite to the phenomenon of WL, where a relatively small magnetic field destroys the constructive quantum interference of scattered electron waves, and hence, reduction in resistance occurs under magnetic field. Further, the presence of a constant slope in $R(T)$ at high magnetic field and at low temperature is the signature of EEI, as evident from Figs. 4(a) and 4(b). Therefore, it is clear from the field-dependent $R(T)$ measurements that EEI in the diffusion channel is the main mechanism behind the observed upturn and the associated resistance peak as appearing in the $R(T)$. Moreover, we have carried out MR measurements at temperature far above T_c to have an idea about the contribution from WL. However, no trace of negative MR, which is the signature of WL, is observed even at temperature above T^*, where the SC fluctuations can be ignored. We have observed positive MR at temperature above T^*, which confirms the presence of EEI rather than WL. The MR at higher temperature for the sample TN10A is shown in Fig. S3 in the SM [24].

Furthermore, from the variation of $T_{\max}$ and T^* with the field, we have constructed a phase diagram which is shown in Fig. 4(d). Here, the extracted temperature points $T_{\max}$ and T^* are observed to shift toward lower temperature under application of a magnetic field, and finally, they meet at $\sim$4.75 T, which is marked as the crossover field from the QCC to the EEI-dominated regime at higher magnetic field.

In addition to the field-dependent $R(T)$ measurements, we have carried out isothermal MR measurements to have insight into the interplay between EEL and the SC fluctuations in the presented disordered SC TiN thin films. In Fig. 5, we have presented MR isotherms for the samples TN10, TN9, and TN8 annealed at 780 °C, and for the rest of the samples (TN4, TN5, TN12, and TN13), the MR isotherms are shown in the SM (Fig. S4) [24]. As mentioned before, T_c is obtained from the QCC fit using Eq. (6), and all the samples for $T > T_c$ show positive MR originating typically from SC fluctuations [31]. With increasing temperature, the MR curves shift toward lower magnetic field, and the effect of the magnetic field gets suppressed. In Fig. 6, we have replotted MR data in terms of magnetoconductance (MC), $G(B) = 1/R_s(B)$, with $R_s(B)$ as the field-dependent sheet resistance. Here, we address mainly three relevant quantum contributions to MC, namely, the AL, MT, and WL. The AL contribution comes from the parallel channel formed by the fluctuating Cooper pairs [9]. The second contribution MT is due to the coherent scattering of electrons formed by fluctuating Cooper pairs before losing their phase coherence [10,11]. Here, AL and MT are the two main contributions to conductivity from SC fluctuations. AL dominates at temperature close to T_c, and MT dominates far above T_c. The third contribution (WL) comes from the constructive quantum interference of scattered electron waves moving in a closed trajectory but opposite in direction [32]. The SC fluctuations (AL and MT) give negative contributions, and WL gives a positive contribution to the MC [31]. Now theoretically, the field-dependent electrical conductance can be expressed as

$$G_{xx}(B, T) = G^n + \Delta G^{\mathrm{SF}}(B, T) + \Delta G^{\mathrm{WL}}(B, T), \quad (7)$$

where the first term denotes Drude's conductance, the second term represents the conductance from SC fluctuations, and the last term originates from disorder-induced quantum interference of scattered electronic waves. Here, as quantum contributions are considered, we omit the classical Drude's conductance from Eq. (7), and the total quantum corrections to the MC can be expressed as

$$\Delta G_{xx}(B, T) = \Delta G^{\mathrm{SF}}(B, T) + \Delta G^{\mathrm{WL}}(B, T). \quad (8)$$

First, we address the contributions to MC from SC fluctuations (AL and MT), and the AL contribution to MC can be expressed as

$$\Delta G^{\mathrm{AL}}(B, T) = G_{00} \frac{\pi^2}{8 \ln\left(\frac{T}{T_c}\right)} \left\{ 8\left(\frac{B_{\mathrm{SF}}}{B}\right)^2 \left[\psi\left(\frac{1}{2} + \frac{B_{\mathrm{SF}}}{B}\right) \right. \right.$$
$$\left. \left. - \psi\left(1 + \frac{B_{\mathrm{SF}}}{B}\right) + \frac{B}{2B_{\mathrm{SF}}} \right] - 1 \right\}, \quad (9)$$

where $\psi(x)$ is the digamma function, B_{SF} is the characteristic field related to SC fluctuations and can be expressed by the GL relaxation time τ_{GL} as $B_{\mathrm{SF}} = \frac{\hbar}{4eD\tau_{\mathrm{GL}}}$ with $\tau_{\mathrm{GL}} = \frac{\pi\hbar}{8K_B T \ln(T/T_c)}$.

Secondly, the MT contribution to MC can be written in terms of $\beta_{\mathrm{LdS}}(T/T_c, \delta)$, which is the magnetic-field-dependent modified electron-electron attraction strength $\beta(T/T_c)$, the extended version of Larkin's $\beta_L(T/T_c)$ parameter that determines the effective EEI strength [16]. Here, δ is the pair-breaking or cutoff parameter [27,31,33]. Lopes dos Santos and Abrahams [17] have extended Larkin's results
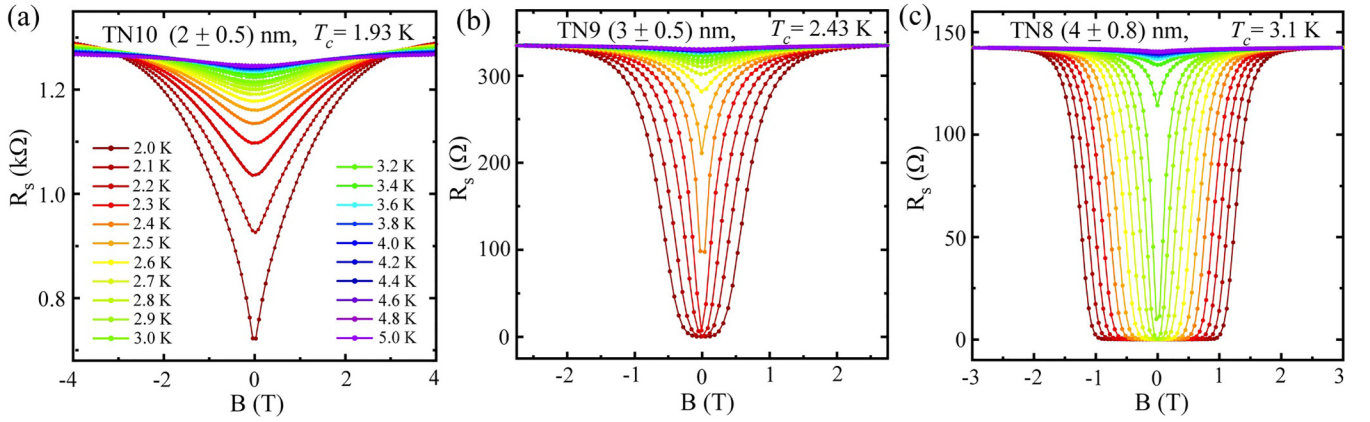
FIG. 5. Magnetoresistance isotherms for the samples (TN10, TN9, and TN8) annealed at 780 °C, and their respective T_c's are obtained through total quantum correction to the conductivity (QCC) fitting.
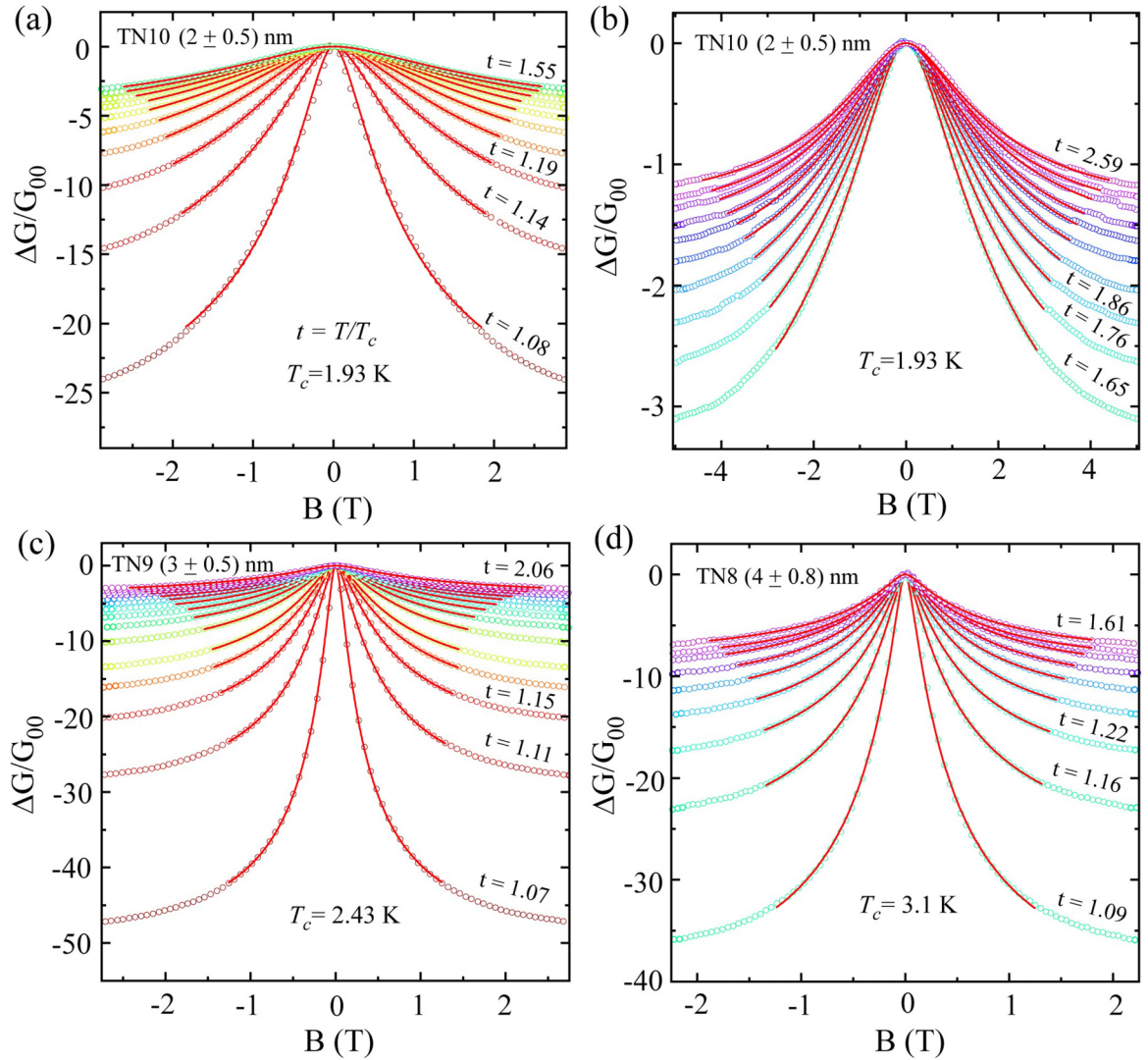

FIG. 6. Magnetoconductance (MC) isotherms for samples (a) and (b) TN10, (c) TN9, and (d) TN8. The red solid curves are the fits obtained by the total quantum corrections to the MC that include mainly superconducting fluctuations [Aslamazov-Larkin (AL) and Maki-Thompson (MT)] and weak localization (WL), as expressed in Eqs. (9), (10), and (12), respectively.

for lower temperatures [close to $\ln(T/T_c) \ll 1$)] and higher magnetic field range ($B \ll k_B T/4eD$) [17,31,33] because Larkin's calculations on the temperature and magnetic field exclude the immediate vicinity of T_c and are subjected to low magnetic field. Therefore, the extended form of MT contribution from Lopes dos Santos and Abrahams [17] can be written as [33]

$$\Delta G^{\mathrm{MT}}(B, T) = -G_1 \frac{e^2}{2\pi^2 \hbar} \left[\psi\left(\frac{1}{2} + \frac{B_\phi}{B}\right) - \psi\left(\frac{1}{2} + \frac{B_{\mathrm{SF}}}{B}\right) + \ln\left(\frac{B_{\mathrm{SF}}}{B_\phi}\right) \right], \quad (10)$$

where

$$G_1 = \beta_{\mathrm{LdS}}\left(\frac{T}{T_C}, \delta\right), \quad \beta_{\mathrm{LdS}}\left(\frac{T}{T_C}, \delta\right) \equiv \frac{\pi^2}{4(\in - \delta)},$$

$$\in \equiv \ln\left(\frac{T}{T_C}\right), \quad \delta = \frac{\pi \hbar}{8 k_B T} \frac{1}{\tau_\phi}. \quad (11)$$

Thirdly, the WL contribution to MC can be written as

$$\Delta G^{\mathrm{WL}}(B, T) = N \frac{e^2}{2\pi^2 \hbar} Y\left(\frac{B}{B_\phi}\right), \quad (12)$$

where

$$Y(x) = \ln(x) + \psi\left(\frac{1}{2} + \frac{1}{x}\right), \quad B_\phi = \frac{\hbar}{4eD\tau_\phi},$$

$$D = \frac{\pi}{2\gamma} \frac{k_B T_C}{e B_{C2}(0)}, \quad \gamma = 1.78. \quad (13)$$

Here, τ_ϕ is the dephasing scattering time, the associated magnetic field (B_ϕ) is known as the phase-breaking field, and D is the diffusion constant. The coefficient N in Eq. (12) represents the number of channels participating in the conduction process [28]. Further, we have calculated MC from the measured longitudinal MR with resistance in Ω/sq by using the given expression:

$$\Delta G_{xx}(B) = \frac{1}{R_{xx}(B)} - \frac{1}{R_{xx}(0)} = -\frac{R_{xx}(B) - R_{xx}(0)}{R_{xx}(B) R_{xx}(0)}, \quad (14)$$

and have plotted them in units of $G_{00} = \frac{e^2}{2\pi^2 \hbar}$ as $\Delta G_{xx}(B)/G_{00}$ in Fig. 6.

Here, we have taken care of the dimensionality as discussed above and validity of the MT expression ($B \ll k_B T/4eD$) in selecting the magnetic field range for fitting the experimental data shown in Fig. 6. Combining the AL, MT, and WL contributions by using Eqs. (9), (10), and (12), respectively, we have fitted the experimental MC for temperature above T_c, i.e., $t > 1$, where $t = T/T_c$ is the reduced temperature. For the fits as shown by the red solid curves in Fig. 6, the characteristic fields B_ϕ and B_{SF} have been used as the free parameters, and $\beta_{\mathrm{LdS}}(T/T_c, \delta)$ is exactly taken as it is expressed in Eq. (11). The fits show excellent agreement with the experimental data, as shown in Fig. 6. For a clearer view, the MC isotherms for the sample TN10 are split into two sets based on the temperature range. The set with t in the range from 1.08 to 1.55 is shown in Fig. 6(a), and the second set up to $t = 2.59$ is shown in Fig. 6(b). For

TN9 and TN8, the MC data along with the fits are presented in Figs. 6(c) and 6(d), respectively. The MC curves and the corresponding fits for the rest of the samples belonging to T_a (820 and 750 °C) are shown in the SM (Fig. S5) [24]. From the fit, τ_ϕ has been extracted through the phase-breaking field B_ϕ. Further, the coefficient for the MT contribution to the MC, $\beta_{\mathrm{LdS}}(T/T_c, \delta)$, as expressed in Eqs. (10) and (11), relates with τ_ϕ via the pair-breaking parameter δ. For all the samples, we have evaluated the inverse phase scattering time (τ_ϕ^{-1}) and $\beta_{\mathrm{LdS}}(T/T_c, \delta)$, and they have been plotted with respect to the reduced temperature T/T_c in Fig. 7. Here, $\beta_{\mathrm{LdS}}(T/T_c, \delta)$ is the parameter introduced by Lopes dos Santos and Abrahams [17] in the modified version of Larkin's theory. The extended version of the theory is valid for the temperature points close to T_c, where $\ln(T/T_c) \ll 1$. In our case, all the temperature points are adhered to the condition mentioned for the validity of the extended version of Larkin's theory [17]. In the limit, $\ln(T/T_c) \ll 1$, $\beta_{\mathrm{LdS}}(T/T_c, \delta)$ takes the form as mentioned in Eq. (11) and depends on τ_ϕ values. Interestingly, the variations of $\beta_{\mathrm{LdS}}(T/T_c, \delta)$ on the reduced temperature, as observed in Fig. 7(a), merge on top of each other for all the measured samples presented in this paper. Hence, the dependence of $\beta_{\mathrm{LdS}}(T/T_c, \delta)$ on the reduced temperature follows a unanimous trend and does not depend on the growth parameters if the two-dimensionality is maintained. In this case, the growth parameters are mainly the annealing temperature (T_a) and the sample thickness (d). As evident in Fig. 7(a), the variation of $\beta_{\mathrm{LdS}}(T/T_c, \delta)$ shows weak dependence or becomes almost independent of temperature for $T/T_c > 1.5$, and it diverges as T approaches T_c. To have the confirmation of this generalized trend in the dependence of $\beta_{\mathrm{LdS}}(T/T_c, \delta)$ on the reduced temperature, the inset of Fig. 7(a) magnifies the diverging part of $\beta_{\mathrm{LdS}}(T/T_c, \delta)$ close to T_c, and indeed, all the samples follow the common path in the plot.

Furthermore, the extracted values of B_ϕ from the MC fitting are converted into τ_ϕ by using the expression $B_\phi = \frac{\hbar}{4eD\tau_\phi}$ for all the TiN samples, and they are presented as inverse phase scattering time (τ_ϕ^{-1}) with respect to the reduced temperature in Fig. 7(b). Here also, we observe that the samples follow a general trend with two distinct regions with clear variation of the slopes that are highlighted by two different shades. The first region, as highlighted by the cyan shade (close to T_c), shows an abrupt decrement in τ_ϕ^{-1} as temperature approaches T_c from high temperature. The second region highlighted in light green for $T/T_c > 1.17$ demonstrates a linear variation of τ_ϕ^{-1} with temperature. Generally, there are three inelastic scattering mechanisms that lead to the phase relaxation in 2D superconductors in the dirty limit, and the corresponding scattering rates are (i) the electron-phonon scattering rate $\tau_{\mathrm{e-ph}}^{-1}$, (ii) the inelastic electron-electron scattering rate $\tau_{\mathrm{e-e}}^{-1}$, and (iii) the inelastic scattering rate of electrons due to SC fluctuations $\tau_{\mathrm{e-fl}}^{-1}$ [34]. The electron-phonon scattering rate ($\tau_{\mathrm{e-ph}}^{-1} \propto T^3$) is mainly prominent at high temperature [27,35]. As the magnetotransport study presented in this paper has been carried out for the temperature range $T \leqslant 2.5 T_c$, where SC fluctuations and EEI mechanisms are dominant, the electron-phonon scattering can be ignored [13]. Further, for a dirty superconductor in the 2D limit where the thermal diffusion length is more than the sample thickness (which is
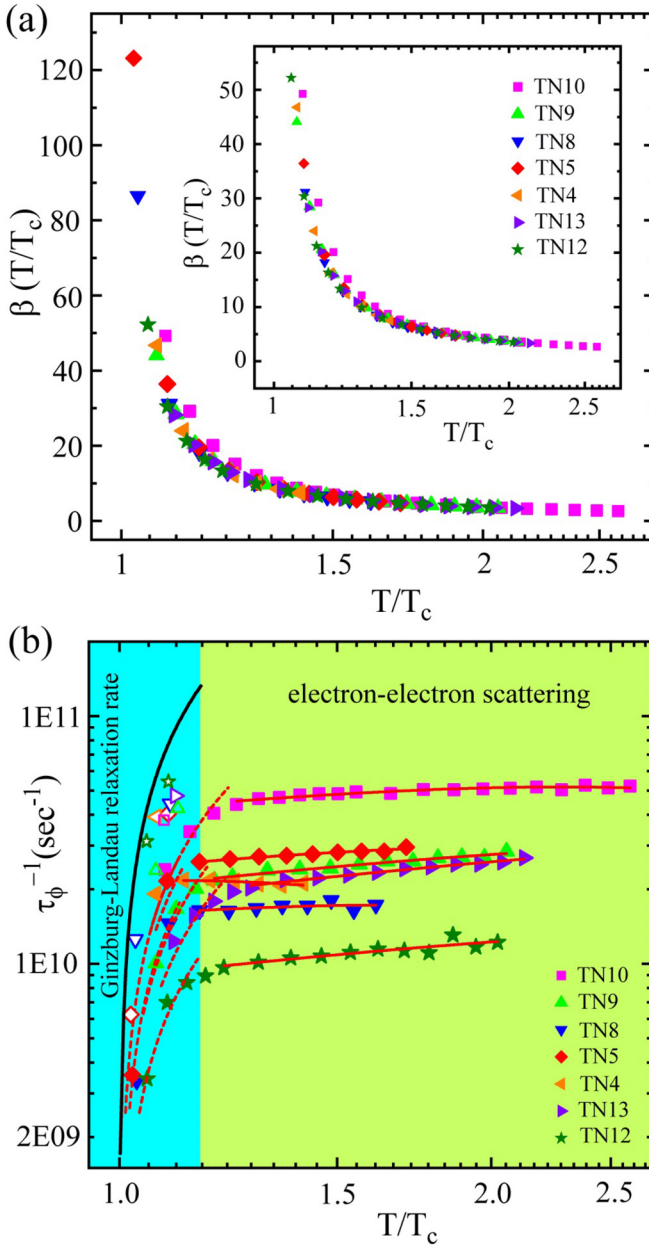
FIG. 7. Dependence of modified Larkin's parameter $\beta_{\mathrm{LdS}}(T/T_c, \delta)$ and inverse phase scattering time (τ_ϕ^{-1}) on reduced temperature T/T_c. (a) A semilogarithmic presentation of the variation of $\beta_{\mathrm{LdS}}(T/T_c, \delta)$ with reduced temperature (T/T_c) for all the TiN samples presented in this paper from different batches annealed at 820, 780, and 750 °C and with different film thickness. The inset shows the magnified view of $\beta_{\mathrm{LdS}}(T/T_c, \delta)$ variation with the reduced temperature for T close to T_c. (b) Logarithmic plot of inverse phase scattering time (τ_ϕ^{-1}) with reduced temperature for all the measured TiN samples. The red dashed curves correspond to $\tau_\phi^{-1} \propto (T - T_c)$, the black solid curve represents the Ginzburg-Landau relaxation rate $\tau_{\mathrm{GL}}^{-1} = (8k_B/\pi\hbar)(T - T_c)$ with $T_c = 2.43$ K, and the solid red curves are the fits using Eq. (15) for inverse electron-electron scattering time. The open symbols represent the inverse characteristic time obtained from the characteristic field B_{SF}.

the case for the present set of samples as listed in Table I), the inelastic electron-electron scattering rate $\tau_{\mathrm{e-e}}^{-1}$ varies linearly with temperature according to the expression [13,34]:

$$\tau_{\mathrm{e-e}}^{-1} = \frac{e^2 R}{2\pi\hbar^2} k_B T \ln\frac{\pi\hbar}{e^2 R}. \tag{15}$$

The experimental data points show excellent agreement with the theoretical expression given in Eq. (15) for inelastic electron-electron scattering, as shown by the red solid curves in Fig. 7(b) in the light green shaded region. However, the region below 1.17 T_c (in cyan shade) shows a strong downturn in the phase scattering rate τ_ϕ^{-1}.

As the temperature approaches T_c, the inelastic scattering of electrons due to SC fluctuations becomes prominent, and the electron-fluctuation rate $\tau_{\mathrm{e-fl}}^{-1}$ is given by [36,37]

$$\tau_{\mathrm{e-fl}}^{-1} = \frac{e^2 R_s}{2\pi\hbar^2} k_B T \frac{2\ln 2}{\ln\frac{T}{T_c} + D}, \quad \text{with}$$

$$D = \frac{4\ln 2}{\sqrt{\ln^2\left(\frac{\pi\hbar}{e^2 R_s}\right) + \frac{128\hbar}{e^2 R}} - \ln\left(\frac{\pi\hbar}{e^2 R_s}\right)}. \tag{16}$$

According to Eq. (16), a strong upturn in the temperature dependence of τ_ϕ^{-1} at T very close to T_c is predicted as $\ln(T/T_c)$ in the denominator of the $\tau_{\mathrm{e-fl}}^{-1}$ term becomes almost zero. However, here, in this paper, we observe a strong downturn in τ_ϕ^{-1} as the temperature approaches T_c from higher temperature. Similar behavior of τ_ϕ^{-1} near T_c has been also observed for In/InO$_x$ composite films [38], Re$_{70}$W$_{30}$, and Nb$_{1-x}$Ta$_x$ thin films [39,40]. The phase relaxation rate τ_ϕ^{-1} in this regime varies proportionally to $(T - T_c)$, as shown by the red dashed curves in Fig. 7(b), in a similar fashion as that of the GL phase relaxation rate $\tau_{\mathrm{GL}}^{-1} = (8k_B/\pi\hbar)(T - T_c)$ at T very close to T_c [40].

In the immediate vicinity of T_c, the resemblance in temperature variation of τ_ϕ^{-1} with that of τ_{GL}^{-1} can be understood from the AL contribution which is one of the most prominent contributions to the MC near T_c [41]. The AL term is fundamentally different from the other terms, as the only characteristic field B_{SF} [Eq. (9)] used in the AL term is different than the characteristic dephasing field B_ϕ used in other terms [41]. The characteristic field B_{SF} is associated with the GL time $\tau_{\mathrm{GL}} = \frac{\pi\hbar}{8k_B T \ln(T/T_c)}$ [40]. Hence, the phase relaxation rate τ_ϕ^{-1} obtained from the AL term near T_c can measure the GL phase relaxation rate τ_{GL}^{-1} [40]. In Fig. 7(b), the solid black curve for $T/T_c < 1.17$ represents the τ_{GL}^{-1} for $T_c = 2.43$ K, and the open symbols represent the inverse characteristic time related to B_{SF}. It is clear from the figure that the phase relaxation rate related to B_{SF} closely follows the GL phase relaxation rate τ_{GL}^{-1} for the set of samples presented in Table I. The deviation for the experimental points from the GL rate τ_{GL}^{-1} as appearing in Fig. 7(b) can originate from some contributions from normal electrons that are modified due to SC fluctuations near the transition [42]. Therefore, clearly, the first regime with steeper slope relates to dephasing caused by SC fluctuations, whereas the second regime corresponds to inelastic electron-electron

scattering–induced dephasing, and all the samples offer the generic trend as evident in Fig. 7(b).

IV. CONCLUSIONS

To summarize, we have revisited the QCC terms for disordered 2D SC TiN thin films. We observe a strong interplay between the SC fluctuations and EEIs. The $R(T)$ measurements, carried out under zero magnetic field, feature different regimes that are mainly defined by the sign of the slope dR/dT. Transitions from metallic to weak insulating and further to the SC regime are obtained for the samples while cooling down from room temperature to 2 K. Despite having different growth conditions such as annealing temperature and film thickness, all the samples presented in this paper follow a similar trend in their zero-field $R(T)$ characteristics that feature a resistance dip at the end of the metallic state, an upturn along with a resistance peak indicating a weak insulating state, and finally, a sharp drop in the resistance due to the onset of superconductivity. We have shown that the intermediate upturn and hence the weak-insulating type of behavior in the zero-field $R(T)$ is mainly due to the EEI which is further supported by the field-dependent $R(T)$. However, the samples presented here are of low resistance ($<1.5\,\mathrm{k\Omega}$) values, and hence, the observed upturns are also weak. To observe a stronger upturn, we have measured a highly resistive sample with $R_{\max} \sim 18\,\mathrm{k\Omega}$ which eventually offers a much stronger upturn in the zero-field $R(T)$. The results from the zero-field $R(T)$ and $R(T)$ under external magnetic field (Fig. S6 in the SM [24]) are consistent with that obtained from the low resistive samples presented here.

Here, WL does not play any significant role as supported by the MR measurements also. Further, from the analysis of AL, MT, and WL contributions to the MC, we have investigated the variations of the modified Larkin parameter $\beta(T/T_c)$ and the inverse phase relaxation time (τ_ϕ^{-1}) on the reduced temperature (T/T_c), and both show a generic pattern which all the samples follow very closely.

[1] M. R. Beasley, J. E. Mooij, and T. P. Orlando, Phys. Rev. Lett. **42**, 1165 (1979).

[2] B. I. Halperin and D. R. Nelson, J. Low Temp. Phys. **36**, 599 (1979).

[3] L. Benfatto, C. Castellani, and T. Giamarchi, Phys. Rev. B **80**, 214506 (2009).

[4] B. Altshuler and A. G. Aronov, in *Electron-Electron Interactions in Disordered Systems*, edited by A. L. Efros and M. Pollak (North-Holland, Amsterdam, 1985), pp. 1–155.

[5] A. Larkin and A. Varlamov, *Theory of Fluctuations in Superconductors* (Oxford University Press, Oxford, 2005).

[6] E. Abrahams, P. W. Anderson, D. C. Licciardello, and T. V. Ramakrishnan, Phys. Rev. Lett. **42**, 673 (1979).

[7] B. L. Altshuler, A. G. Aronov, and P. A. Lee, Phys. Rev. Lett. **44**, 1288 (1980).

[8] P. A. Lee and T. V. Ramakrishnan, Rev. Mod. Phys. **57**, 287 (1985).

[9] L. G. Aslamasov and A. I. Larkin, Phys. Lett. A **26**, 238 (1968).

[10] K. Maki, Prog. Theor. Phys. **39**, 897 (1968).

[11] R. S. Thompson, Phys. Rev. B **1**, 327 (1970).

[12] B. Sacépé, C. Chapelier, T. I. Baturina, V. M. Vinokur, M. R. Baklanov, and M. Sanquer, Nat. Commun. **1**, 140 (2010).

[13] T. I. Baturina, S. V. Postolova, A. Y. Mironov, A. Glatz, M. R. Baklanov, and V. M. Vinokur, Europhys. Lett. **97**, 17012 (2012).

[14] T. A. Dauzhenka, V. K. Ksenevich, I. A. Bashmakov, and J. Galibert, Phys. Rev. B **83**, 165309 (2011).

[15] H. Xue, Y. Hong, C. Li, J. Meng, Y. Li, K. Liu, M. Liu, W. Jiang, Z. Zhang, L. He *et al.*, Phys. Rev. B **98**, 085305 (2018).

[16] A. Larkin, Pis'ma Zh. Eksp. Teor. Fiz. **31**, 239 (1980) [JETP Lett. **31**, 219 (1980)].

[17] J. M. B. Lopes dos Santos and E. Abrahams, Phys. Rev. B **31**, 172 (1985).

[18] S. Yadav, A. Sharma, B. Gajar, M. Kaur, D. Singh, S. Singh, K. K. Maurya, S. Husale, V. N. Ojha, and S. Sahoo, Adv. Eng. Mater. **21**, 1900061 (2019).

[19] S. Yadav, V. Kaushik, M. P. Saravanan, R. P. Aloysius, V. Ganesan, and S. Sahoo, Sci. Rep. **11**, 7888 (2021).

[20] S. Yadav and S. Sahoo, Appl. Surf. Sci. **541**, 148465 (2021).

[21] B. Gajar, S. Yadav, D. Sawle, K. K. Maurya, A. Gupta, R. P. Aloysius, and S. Sahoo, Sci. Rep. **9**, 8811 (2019).

[22] J. M. Valles and R. C. Dynes, MRS Proc. **195**, 375 (1990).

[23] D. Belitz and T. R. Kirkpatrick, Rev. Mod. Phys. **66**, 261 (1994).

[24] See Supplemental Material at http://link.aps.org/supplemental/10.1103/PhysRevB.107.014511 for a similar analysis of zero-field $R(T)$ and MC data obtained from four more samples, high-temperature MR data, fitting parameters from the QCC fit to the zero-field $R(T)$, and data from a highly resistive sample and AFM images.

[25] H.-B. Jang, J. S. Lim, and C.-H. Yang, Sci. Rep. **10**, 3236 (2020).

[26] S. V. Postolova, A. Y. Mironov, M. R. Baklanov, V. M. Vinokur, and T. I. Baturina, Sci. Rep. **7**, 1718 (2017).

[27] M. Giannouri, E. Rocofyllou, C. Papastaikoudis, and W. Schilling, Phys. Rev. B **56**, 6148 (1997).

[28] J. Wang, W. Powers, Z. Zhang, M. Smith, B. J. McIntosh, S. K. Bac, L. Riney, M. Zhukovskyi, T. Orlova, L. P. Rokhinson *et al.*, Nano Lett. **22**, 792 (2022).

[29] P. A. Lee and T. V. Ramakrishnan, Phys. Rev. B **26**, 4009 (1982).

[30] J. Wang, A. M. DaSilva, C.-Z. Chang, K. He, J. K. Jain, N. Samarth, X.-C. Ma, Q.-K. Xue, and M. H. W. Chan, Phys. Rev. B **83**, 245438 (2011).

[31] A. Y. Mironov, S. V. Postolova, and T. I. Baturina, J. Phys.: Condens. Matter **30**, 485601 (2018).

[32] G. Bergmann, Phys. Rep. **107**, 1 (1984).

[33] N. P. Breznay and A. Kapitulnik, Phys. Rev. B **88**, 104510 (2013).

[34] X. Zhang, A. E. Lita, M. Sidorova, V. B. Verma, Q. Wang, S. W. Nam, A. Semenov, and A. Schilling, Phys, Rev. B **97**, 174502 (2018).

[35] X. Zhang, A. Engel, Q. Wang, A. Schilling, A. Semenov, M. Sidorova, H. W. Hübers, I. Charaev, K. Ilin, and M. Siegel, Phys. Rev. B **94**, 174509 (2016).

[36] W. Brenig, M.-C. Chang, E. Abrahams, and P. Wölfle, Phys. Rev. B **31**, 7001 (1985).

[37] W. Brenig, M. A. Paalanen, A. F. Hebard, and P. Wölfle, Phys. Rev. B **33**, 1691 (1986).

[38] A. F. Hebard and M. A. Paalanen, Phys. Rev. B **30**, 4063 (1984).

[39] H. Raffy and R. B. Laibowitz, Phys. Rev. B **30**, 5541 (1984).

[40] M. Giannouri, C. Papastaikoudis, and R. Rosenbaum, Phys. Rev. B **59**, 4463 (1999).

[41] J. M. Gordon, C. J. Lobb, and M. Tinkham, Phys. Rev. B **29**, 5232 (1984).

[42] M. H. Redi, Phys. Rev. B **16**, 2027 (1977).